

Collisional effects in the blue wing of the Balmer- α line[★]

N. F. Allard^{1,2★★}, F. Spiegelman³, J. F. Kielkopf⁴, and S. Bourdoux²

¹ GEPI, Observatoire de Paris, Université PSL, UMR 8111, CNRS, 61, Avenue de l'Observatoire, F-75014 Paris, France
e-mail: nicole.allard@obspm.fr

² Sorbonne Université, CNRS, UMR7095, Institut d'Astrophysique de Paris, 98bis Boulevard Arago, Paris, France

³ Laboratoire de Physique et Chimie Quantique, Fédération FERMI, Université de Toulouse (UPS) and CNRS, 118 route de Narbonne, F-31400 Toulouse, France

⁴ Department of Physics and Astronomy, University of Louisville, Louisville, Kentucky 40292 USA

Received 3june2021 / Accepted 20september2021;

ABSTRACT

In order to investigate the near wing of the Lyman- α line, accurate line profile calculations and molecular data are both required due to the existence of a close line satellite responsible for its asymmetrical shape. Lyman- α lines observed with the *Cosmic Origin Spectrograph* (COS) on the *Hubble Space Telescope* (HST) show this peculiarity in the spectra of DBA and DA white dwarf stars. A similar asymmetrical shape in the blue wing can be predicted in the Balmer- α line of H perturbed by He and H atoms.

In continuation with a very recent work on the Lyman- α line, where the $n = 2$ potential energies and transition dipole moments from the ground state were determined, we present new accurate H-He potential energies and electronic transition dipole moments involving the molecular states correlated with H($n=3$)+He and their transition dipole moments with the states correlated with H($n=2$)+He. Those new data and existing molecular data for H($n=2,3$)-H are used to provide a theoretical investigation of the collisional effects in the blue wing of the Balmer- α line of H perturbed by He and H atoms. We note the consequences for the Balmer- α line shape in the physical conditions found in the cool atmosphere of DZA white dwarfs where helium densities may be as high as 10^{21} cm⁻³. This study is undertaken with a unified theory of spectral line broadening valid at very high helium densities.

Key words. star - white dwarf - spectrum - spectral line

1. Introduction

Accurate atomic and molecular data, both theoretical and experimental, are required to fully exploit current and future astrophysical space missions and ground-based facilities that deliver sensitive precise spectroscopy. Through the comparison of spectroscopic observations with models based on our best physics we gain an understanding of the composition, temperature, density, magnetic fields, turbulence, and motions of the objects of interest. An example, which is the key point of this paper, is the decades-old problem of the determination of the hydrogen abundance in helium-dominated white dwarf stars (Cukanovaite et al. 2021). There is a discrepancy in the hydrogen abundance determined from optical spectra of Balmer- α and the abundance determined from ultraviolet spectra of Lyman- α that is possibly due to calculated opacities for these lines that have been incorporated into stellar atmosphere code. We have noted previously that there is a reliance on simplified models of neutral atom collision line-broadening physics, some dating to the work of Unsold (1955), in most of the codes that are in current use. The reasons are understandable. Neutral collision broadening depends on the knowledge of neutral atom interactions at separations typically

greater than those at which atoms are stable in molecules. At very large separations the van der Waals interactions that we can model apply and are well-understood, while atoms in stars radiate in the presence of other atoms that are closer than this. It is only relatively recently that the ab initio methodology for computing energies of atom pairs has developed the extreme precision needed to provide these data, especially for excited states. Consequently, potential energy models had been adopted that used ad hoc choices that were not validated in the laboratory. For the determination of abundances, it is important that the Lyman- α and Balmer- α lines be fully resolved in low-noise observations, and be adequately represented in the theoretical models that are applied to them. The use of Lorentzian profiles with different widths predicted by the hydrogenic van der Waals approximation is inadequate to the task, as was emphasized before by Allard et al. (2007) and Peach (2011). While an accurate determination of the resonance broadening of Balmer- α has been achieved by Allard et al. (2008), nothing comparable exists for H-He. The calculations reported in Allard et al. (2008) support the results of Barklem et al. (2000a, 2002) that the Ali & Griem (1966) theory of atom-atom resonance broadening for hydrogen underestimates the actual line width. This will be the topic of a forthcoming paper; the present work is focussed on the blue wing of the Balmer- α and its asymmetrical shape due to radiation during close collisions.

[★] Opacity tables are only available at the CDS via anonymous ftp to cdsarc.u-strasbg.fr (130.79.128.5)

^{★★} This paper is dedicated to the memory of Annie Spielfiedel and Roger Cayrel for their fundamental work, rigor and kindness

Table 1. Comparison of calculated and experimental atomic energy levels of hydrogen (in cm^{-1}) for the $n=2$ and $n=3$ configurations

level	Coulomb/DKH	Coulomb/DKH/mass	experimental
1s	0	0	0
2s	82303.923	82259.124	82258.954
2p	82304.240	82259.440	82259.163
3s	97545.453	97492.357	97 492.222
3p	97545.607	97492.511	97492.293
3d	97545.773	97492.678	97492.341

Column 2: Theoretical levels including the DKH contribution. Column 3: Theoretical levels with the DKH contribution and finite proton mass correction. The experimental data in Col. 4 correspond to averages over the j spin-orbit terms (weighted by $2j + 1$) taken from Kramida et al. (2020).

In helium-dominated white dwarfs, the Lyman- α line profile is asymmetric (see Xu et al. 2017, and references therein). The existence of a quasi-molecular line satellite is crucial to understanding the asymmetrical shape of the Lyman- α line observed with the *Cosmic Origin Spectrograph* (COS) on the *Hubble Space Telescope* (HST) (see Fig. 1 in Allard et al. 2020). The resonance broadening of hydrogen perturbed by collisions with H atoms produces asymmetry in the Lyman- α line profile similar to that due to H-He. In a recent work, we investigated the absorption features in the blue wings by computing detailed collisional broadening profiles (Spiegelman et al. 2021) for both H-He and H-H using new Multi-Reference Configuration Interaction (MRCI) calculations of the excited states potential energy curves of H-He dissociating into $\text{H}(n=2)+\text{He}$, as well as the relevant electric dipole transition moments from the ground state contributing to the Lyman- α spectrum. We showed that tiny relativistic effects can affect the asymptotic correlation of the H-He adiabatic states and change the related transition dipole moments at intermediate and long distance, significantly affecting the line profile.

In this work we report accurate potential energy curves and transition dipole moments of H-He involving initial and final states correlated with $\text{H}(n=2)+\text{He}$ and $\text{H}(n=3)+\text{He}$, respectively. Between these states, 16 H-He transitions generate the complete Balmer- α line profile. Although all of them were investigated for the present study, we restrict our discussion to the molecular data of the $\Sigma - \Sigma$ transitions which provide the essential contribution to the blue wing (Sect. 2), and we concentrate on the calculation of the asymmetrical shape of the Balmer- α line perturbed by He (Sect. 3) and H atoms (Sect. 4). In Sect. 5 we analyze the general trend of the repulsive Σ excited states which should lead to a non-Lorentzian shape of the Balmer lines when we consider higher orders of the Balmer series in helium-rich white dwarfs.

2. Diatomic H-He potentials and electronic transition dipole moments

The calculation scheme for the potentials dissociating into $\text{H}(n=2,3,4)+\text{He}$ was described in our recent publication dealing with the Lyman- α line broadening (Spiegelman et al. 2021). Briefly, a MRCI calculation (Knowles & Werner 1992; Werner et al. 2015) was run within an extensive Gaussian-type orbital (GTO) basis set, namely 239 GTOs on He and 297 GTOs on H. Scalar relativistic corrections, including the Darwin and the mass-velocity contributions in the Douglas-Kroll-Hess scheme

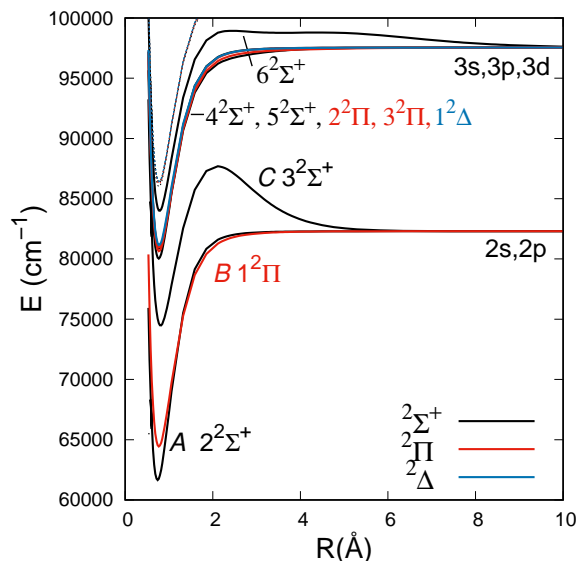


Fig. 1. MRCI adiabatic potential energy curves of HHe molecular states dissociating into $\text{H}(n=2,3)+\text{He}$. The thinner lines at the very top of the plot correspond to potential energy curves of bound states correlated with $\text{H}(n=4)+\text{He}$, not dealt with here.

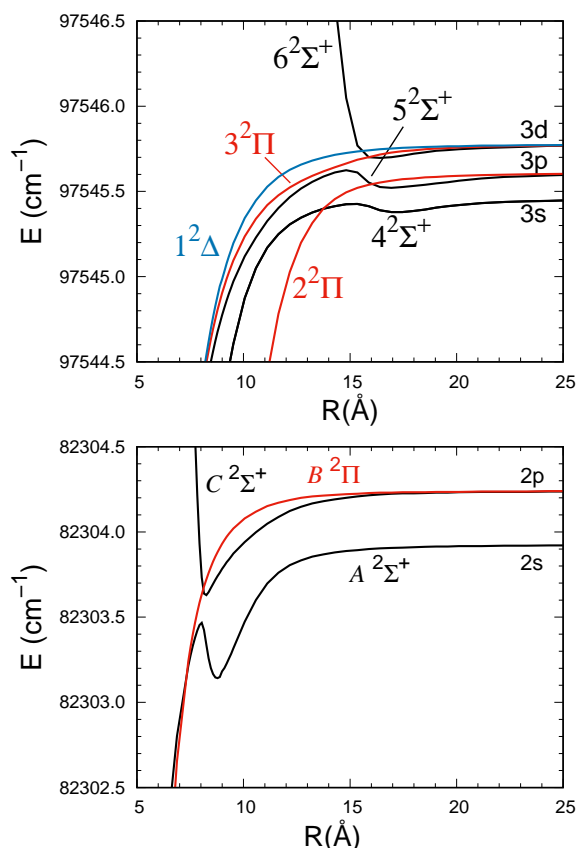


Fig. 2. Zoom-in on the long-range MRCI adiabatic potential energy curves of HHe. Top: States dissociating into $\text{H}(n=3)+\text{He}$. Bottom: States dissociating into $\text{H}(n=2)+\text{He}$.

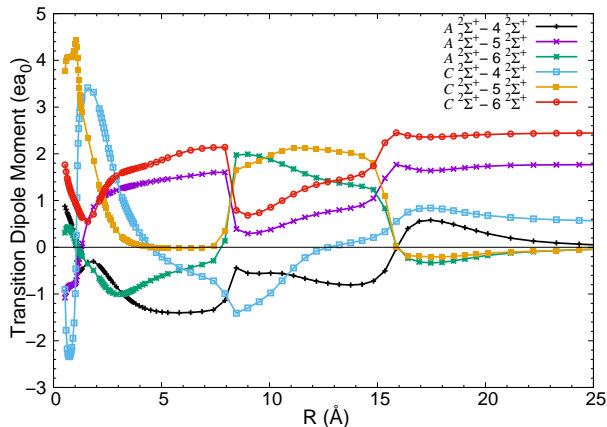


Fig. 3. Transition dipole moments of H-He between $2\Sigma^+$ states $n=2$ and $n=3$.

(DKH) at second order (Reiher 2006; Nakajima & Hirao 2011) were added, breaking the specific degeneracy of the atomic hydrogen levels determined with the Coulomb Hamiltonian only. We showed in our previous work (Spiegelman et al. 2021) that although their influence on the energy was less than 1 cm^{-1} , accounting for relativistic effects could induce long-distance avoided crossings, in turn resulting in changes in the asymptotic correlation of the adiabatic states and in the dipole transition moments. Table 1 shows that the basis set used for the $n = 2$ and $n = 3$ describes the energy levels of hydrogen with an accuracy better than 0.5 cm^{-1} compared to the j -averaged experimental levels deduced from Kramida et al. (2020). In the case of the H-He system, all energy eigenvalues and eigenstates were obtained up to H($n=4$)+He (the $n=4$ manifold is not discussed here).

In the following we use the spectroscopist's notations X , A , B , and C for the lower adiabatic molecular states of H-He, namely the ground state $1^2\Sigma^+$ and the lowest excited states $2^2\Sigma^+$, $1^2\Pi$, and $3^2\Sigma^+$ correlated with H($n=2$)+He, while we will label the upper states correlated with H($n=3$)+He according to their adiabatic ranking in their respective symmetries. In the literature, states $4^2\Sigma^+$, $2^2\Pi$, and $5^2\Sigma^+$ are also labeled D , E , and F , respectively. Figure 1 shows the potential energy curves of the states dissociating into H($n=2$)+He and H($n=3$)+He. The lowest excited states ($n=2$) were abundantly discussed by Theodorakopoulos et al. (1987), Ketterle et al. (1985), Ketterle et al. (1988), Brooks & Hunt (1988), Ketterle (1989), van Hemert & Peyerimhoff (1991), Petsalakis et al. (1990), Sarpal et al. (1991), Lo et al. (2006), Allard et al. (2020) and Spiegelman et al. (2021).

The three states A , B , and C are bound at short distance ($R_e \approx 0.75 \text{ \AA}$ for states A and B with respective dissociation energies 20758 and 17868 cm^{-1}), however, with a smaller dissociation energy ($D_e=13665 \text{ cm}^{-1}$) and a slightly larger equilibrium distance ($R_e=0.8093 \text{ \AA}$) for state $C^2\Sigma^+$, correlatively with a large potential energy barrier to dissociation (data taken from Spiegelman et al. 2021). States dissociating into H($n=3$)+He have a similar behavior; specifically, all states are bound with essentially parallel potential energy curves having equilibrium distances R_e around 0.77 \AA and dissociation energies D_e in the range 16300 – 17600 cm^{-1} . However, the highest state $6^2\Sigma^+$ is peculiar. It has a long-distance barrier and is significantly less bound ($D_e=13554 \text{ cm}^{-1}$) than the former states and at slightly larger distance $R_e=0.7851 \text{ \AA}$. Starting from dissociation, the bar-

rier becomes significant below 10 \AA and extends over a large range down to 1.5 \AA . It presents a double hump structure, the inner maximum being the highest one (1390 cm^{-1} above the asymptote around $R=2.1 \text{ \AA}$), significantly lower than that of the $C^2\Sigma^+$ state correlated with He($2p$)+He (5386 cm^{-1} above the asymptote around $R=1.90 \text{ \AA}$). Detailed adiabatic correlation of the molecular states of H-He towards the atomic states is illustrated in the magnified image in Fig. 2 (top panel) showing the long-distance behavior of the potential curves. In the range 14 – 16 \AA , states $4^2\Sigma^+$, $5^2\Sigma^+$, and $6^2\Sigma^+$ undergo sequential avoided crossings and also crossings with states $2^2\Pi$, $3^2\Pi$, and $1^2\Delta$. Although more states are involved in the $n=3$ manifold, the situation is similar to that of the H($n=2$)+He states shown in Fig. 2 (bottom panel) where the crossings occur at around 8.1 \AA . The spectroscopic constants of the adiabatic states are given in the Appendix and are compared with the literature values (Theodorakopoulos et al. 1987; Sarpal et al. 1991; Ketterle et al. 1985, 1988; Ketterle 1989, 1990a,b,c; van Hemert & Peyerimhoff 1991; Lo et al. 2006). The *rms* deviation of the calculated $v' = 0$ to $v'' = 0$ transition energies (T_{00} in the Appendix table) from the experimental values of Ketterle (1990b) is 23 cm^{-1} . No asymptotic shift or any empirical correction has been made for their determination. However, the inter-state non-adiabatic perturbations (van Hemert & Peyerimhoff 1991; Petsalakis et al. 1990) are not accounted for in the present work.

All 16 transition dipole moments between the $n=2$ and $n=3$ adiabatic states were calculated, namely transitions from $A^2\Sigma^+$, $C^2\Sigma^+$ to $4,5,6^2\Sigma^+$ and to $2,3^2\Pi$, and those from $B^2\Pi$ to $4,5,6^2\Sigma^+$, $2,3^2\Pi$ and $1^2\Delta$. In Fig. 3 we focus on the $2\Sigma^+ - 2\Sigma^+$ transition dipole moments since mainly the $C^2\Sigma^+ - 6^2\Sigma^+$ transition is involved in the blue wing contribution, as discussed below. Transition moments start to depart smoothly from their asymptotic values below 25 \AA , as can be seen in Fig. 3. Their evolution with distance can be understood considering features characterizing either the upper or the lower states of the transitions. The first feature is the avoided crossings between $4^2\Sigma^+$, $5^2\Sigma^+$, and $6^2\Sigma^+$ around $R=16 \text{ \AA}$, which causes switches between $A^2\Sigma^+ - 4^2\Sigma^+$, $A^2\Sigma^+ - 5^2\Sigma^+$, and $A^2\Sigma^+ - 6^2\Sigma^+$ dipole moments on the one hand, and between $C^2\Sigma^+ - 4^2\Sigma^+$, $C^2\Sigma^+ - 5^2\Sigma^+$ and $C^2\Sigma^+ - 6^2\Sigma^+$ dipole moments on the other hand. The second feature is the avoided crossing between states $A^2\Sigma^+$ and $C^2\Sigma^+$ around $R=8.1 \text{ \AA}$, which causes sharp switches between $A^2\Sigma^+ - 4^2\Sigma^+$ and $C^2\Sigma^+ - 4^2\Sigma^+$, $A^2\Sigma^+ - 5^2\Sigma^+$ and $C^2\Sigma^+ - 5^2\Sigma^+$, and $A^2\Sigma^+ - 6^2\Sigma^+$ and $C^2\Sigma^+ - 6^2\Sigma^+$, respectively. Finally, we can also observe avoided crossings of states in their repulsive inner branch for $R < 0.7 \text{ \AA}$ that induce abrupt variations in the transition moments.

While relativistic effects, partly taken into account here, obviously play a negligible role on the energies (less than 1 cm^{-1}) and in the transition dipole moment at short distance, they break the asymptotic degeneracy and induce cascade avoided crossings which govern the asymptotic correlation of the adiabatic states and the variation of the dipole transition moments at medium and long distance. For a full spectral account of the perturbation in the line profiles, it would have been interesting to include spin-orbit coupling (spin-orbit coupling is of the same magnitude as the scalar contributions) at the expense of dealing with more molecular transitions, still more complex features in molecular data and possible numerical difficulties in the determination of the collisional profiles. The fact that the energetics of the blue wing of the line investigated in the present paper is dominantly due to transitions between the repulsive Σ states (see below) somewhat legitimates the neglect of spin-orbit coupling for the

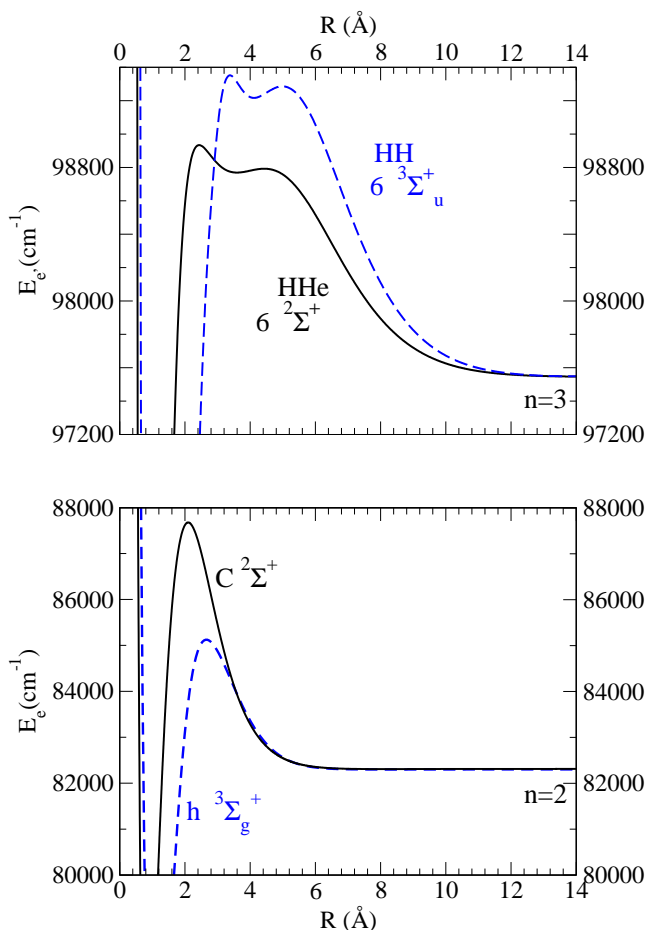


Fig. 4. Upper and lower repulsive potentials of H-He and H-H. Top: Short-range part of the repulsive potential curve $6^2\Sigma^+$ state (black line) of the H-He molecule compared with the $6^3\Sigma_u^+$ state (blue dashed line) of the H-H. Bottom: Short-range part of the potential curves of $C^2\Sigma^+$ state (black line) of the H-He molecule compared with the $h^3\Sigma_g^+$ state (blue dashed line) of H-H. E_e and $E_{e'}$ are the potential energies of the initial ($n=2$) and final ($n=3$) atomic states of the transitions.

line profile calculations, since these repulsive states are always adiabatically correlated with the highest atomic asymptotes for a given n , with or without taking account of fine structure ($2p$ or $2p_{3/2}$ for $n=2$, $3d$ or $3d_{5/2}$ for $n=3$). The evolution of the dipole transition moment between the relevant Σ repulsive states should thus be preserved.

3. Collisional profiles perturbed by He atoms

The potentials and radiative dipole transition moments described above are input data for a unified spectral line shape evaluation of the Balmer line. This treatment includes the finite duration of collision since it is well known that the impact approximation, which assumes that collisions occur instantaneously, causes the Lorentzian approximation to be inaccurate far from the line center. Although our unified theory was developed in Allard et al. (1999), and a detailed discussion is presented there, we provide an overview in Sect. 3 of our preceding paper on the Lyman- α line (Spiegelman et al. 2021). In that paper we focussed on the medium, long distance, and asymptotic limit of the potential curves, and we were able to solve the uncertainty remaining in Allard et al. (2020) involving the adiabatic asymptotic correlation of the Σ states in Lyman- α . The bottom plot of Fig. 2 shows

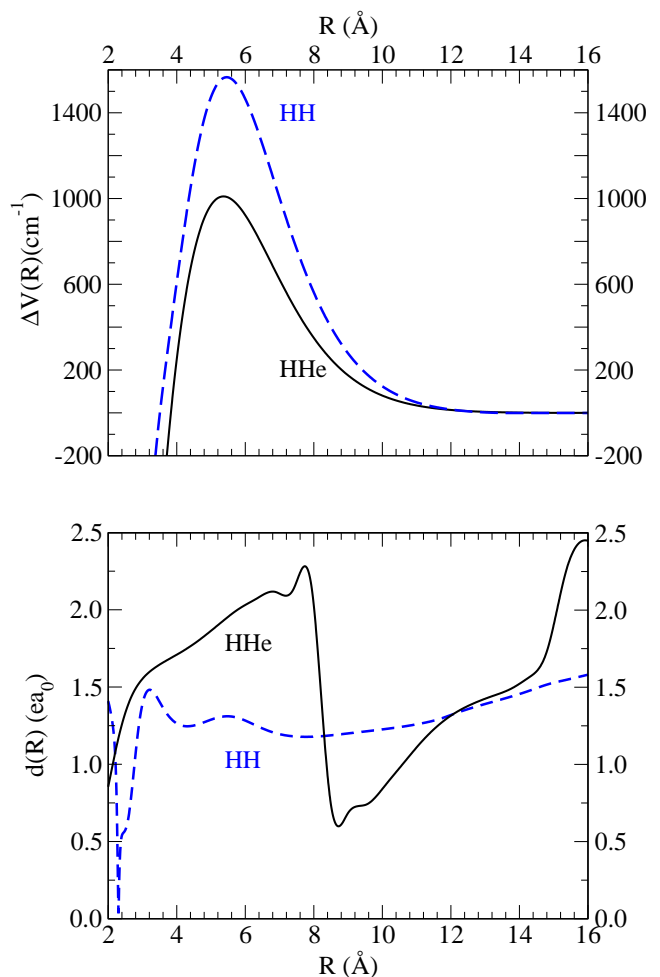


Fig. 5. Difference potentials and electric transition dipole moments related to the repulsive states of H-H and H-He. Top: Difference potential for the triplet transition $6^3\Sigma_u^+ - h^3\Sigma_g^+$ (blue dashed line) of H-H compared with the doublet transition $6^2\Sigma^+ - C^2\Sigma^+$ of H-He (black line). Bottom: Electric dipole moments of the triplet state transition of H-H (blue dashed line) and of the doublet state transition of H-He (black line).

the long-range part of the MRCI adiabatic H-He potential energy curves of states A , B , and C dissociating into $H(n=2) + \text{He}$. As a result of the long-distance avoided crossing around 8.1 \AA in the $2\Sigma^+$ manifold between the $A^2\Sigma^+$ state and the $C^2\Sigma^+$ state, the latter is adiabatically correlated to $2p$. This long-range avoided crossing was also shown to induce a kink at 8.1 \AA in dipole moment $X^2\Sigma^+ - C^2\Sigma^+$ and a sign change in the $X^2\Sigma^+ - A^2\Sigma^+$ dipole transition moment (Fig. 3 in Spiegelman et al. 2021).

Figure 4 shows the short-range part of the potential curve $E_{e'}(R)$ of the repulsive $3d^2\Sigma^+$ state. The prediction of a line satellite in the blue wing of the H-He line profile is related to the potential maximum of $E_{e'}(R)$ in the internuclear distance range $R=2.5\text{--}5.5 \text{ \AA}$. This leads to a maximum of the potential energy difference $\Delta V(R)$ at 5.5 \AA for the $C^2\Sigma^+ \rightarrow 6^2\Sigma^+$ transition. $\Delta V(R)$ shown in Fig. 5 is given by:

$$\Delta V(R) \equiv V_{e'e}(R) = V_{e'}(R) - V_e(R), \quad (1)$$

and represents the difference between the energies of the quasi-molecular transition. The potential energy $V_e(R)$ for a state e is defined as:

$$V_e(R) = E_e(R) - E_e^\infty. \quad (2)$$

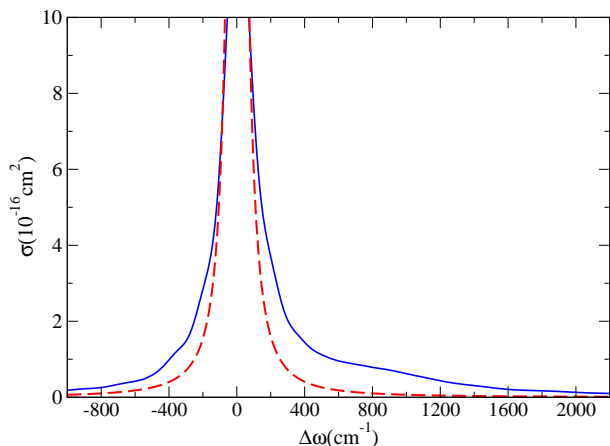


Fig. 6. Comparison of the Balmer- α line perturbed by H-He collisions (blue curve) with the Lorentzian approximation (red dashed curve). The He density is $5 \times 10^{20} \text{ cm}^{-3}$; the temperature is 8000 K.

The unified theory predicts that line satellites will be centered periodically at frequencies corresponding to integer multiples of the extrema of $\Delta V(R)$. The satellite amplitude depends on the value of the electric dipole transition moment through the region of the potential extremum responsible for the satellite and on the position of this extremum (Allard et al. 1998). The electric dipole transition moment is plotted in Fig. 3 and the bottom plot of Fig. 5. The $C^2\Sigma^+ - 6^2\Sigma^+$ transition tends to the asymptotically allowed transition $2p - 3d$. In the present study we consider the temperature and density range of cool DZA white dwarf stars. Figure 6 shows a very broad blue wing with a close line satellite at about 900 cm^{-1} from the line center corresponding to the maximum of $\Delta V(R)$. The deviation from Lorentzian behavior is real, and the asymmetry of the line profile becomes apparent not much farther from the line on the blue short-wavelength side. There is a linear variation in the strength of the blue wing with helium density as long as $n_{\text{He}} \leq 5 \times 10^{20} \text{ cm}^{-3}$; however, when the He density is increased from 5×10^{20} to 10^{21} cm^{-3} the development of the blue wing leads to the center of the main line being overwhelmed by the line satellite. At 10^{21} cm^{-3} the core of the line is shallow and no longer Lorentzian. Figure 7 clearly illustrates how the non-Lorentzian shapes can exist because of the presence of close line satellites. In these physical conditions found in the cool atmosphere of DZA white dwarfs, we are outside the range of validity of the Lorentzian approximation usually used in stellar atmosphere modeling. This clear asymmetry in the wings of the Balmer- α line was noticed by Koester (1995, private communication) in the low-resolution optical spectrum of the DZA white dwarf L745-46A obtained at the ESO La Silla 3.6m telescope. Figure 3 in Koester & Wolff (2000) shows the observed very shallow Balmer- α line with a very broad blue wing.

4. Collisional profiles perturbed by H atoms

We used the non-relativistic ab initio calculations of the H-H potentials of Spielfiedel (2001, private communications), in which the asymptotic states remain degenerate for a given hydrogen quantum number n . Figures 1 and 2 in Allard et al. (2008) show the potential energies correlated to the $3d$ and $2p$ states. Essentially 20 transitions generate the $3d-2p$ H-H component that gives the main contribution to the Balmer- α line broadening.

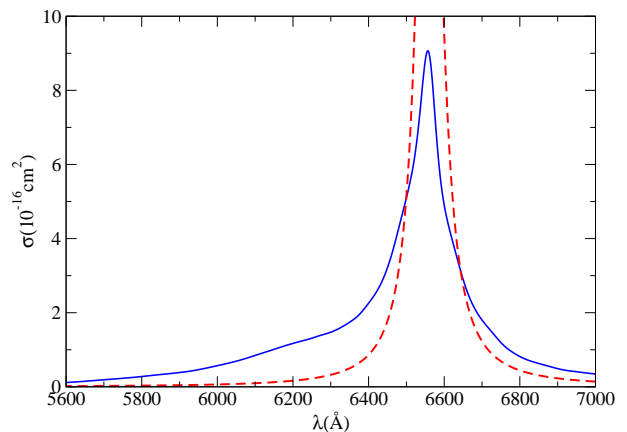


Fig. 7. Comparison of the Balmer- α line perturbed by H-He collisions (blue curve) with the Lorentzian approximation (dashed red curve). The He density is 10^{21} cm^{-3} ; the temperature is 8000 K.

Electronic singlet-singlet and triplet-triplet transition moments of H_2 have already been very well studied by Spielfiedel (2003) and Spielfiedel et al. (2004).

4.1. Self-broadening of the Balmer- α line

In a unified treatment, the complete spectral energy distribution is computed from the core to the far line wing. The Lorentzian widths and shifts can be readily extracted from our unified line broadening calculations (Allard et al. 1999). In Allard et al. (2008), we computed the width and shift of the Balmer- α line perturbed by neutral hydrogen, and studied their dependence on a full range of temperatures from 3000 to 12000 K needed for stellar spectra models. Previous resonance broadening parameters based on a multipole expansion of the interaction, neglecting the van der Waals interactions, had been calculated by Ali & Griem (1966). Their work was widely adopted for use in stellar atmosphere models. Our calculations lead to larger values than those obtained with the commonly used theory of Ali & Griem (1966) and are closer to the calculations of Barklem et al. (2000b) and Barklem et al. (2000a). Using up-to-date theories of the Balmer- α broadening mechanisms, Cayrel et al. (2011) was able to obtain excellent fits of observed stellar Balmer- α profiles with computed profiles, using 1D Kurucz Atlas9 models, in the temperature range from 5000K to 7000 K; the other parameters (metallicity, $[\alpha/\text{Fe}]$, and $\log g$) were fixed by a reliable detailed analysis of the atmosphere. The new values of the collisional self-broadening of Balmer- α have raised a problem that had remained hidden because of the far too small value of the cross-section proposed by Ali-Griem which had been largely used since 1966. The accuracy of the new values excludes the former agreement between observed and computed Balmer- α profiles with 1D models. For Balmer series profiles in the Sun and generally in F, G, and K stars, only 3D radiative hydrodynamical models that rely on fundamental physics are adequate to model accurately the complexities of convection and the emergent line profile (Ludwig et al. 2009; Amarsi et al. 2018; Giribaldi et al. 2019). Moreover, the shift and width of hydrogen Balmer- α at high electron density in a laser-produced plasma reported in Kielkopf & Allard (2014) would suggest that for conditions of white dwarf stars the atomic physics is not completely understood.

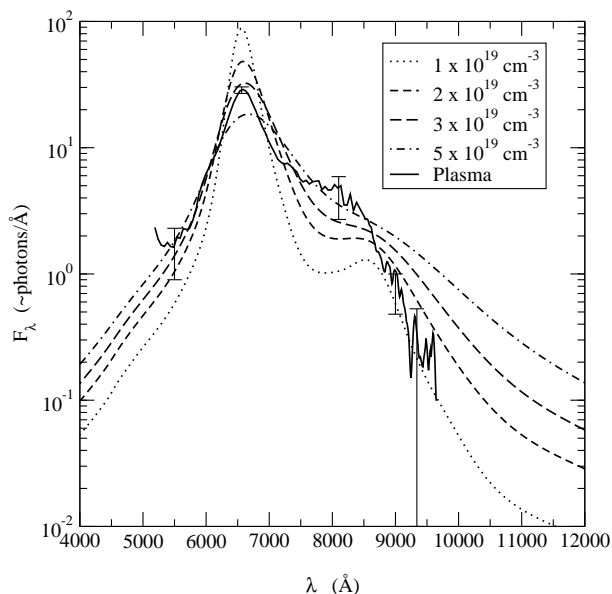


Fig. 8. Comparison of the Balmer- α line as seen in the time-integrated experimental data with theoretical profiles at different ion densities (extracted from Fig. 8 of Kielkopf et al. (2002)). The plasma density is $3 \times 10^{19} \text{ cm}^{-3}$.

4.2. Blue wing of the Balmer- α line

The unified theory of spectral line broadening applied to the Balmer- α line of atomic hydrogen predicts structure in the Balmer- α line wing due to radiation that is emitted during atom-ion collisions. The strongest feature is a satellite at 8650 Å. Laboratory observations of a laser-produced hydrogen plasma confirm that prediction (Kielkopf et al. 2002). In Fig. 8 we compare the theoretical profiles in the region of the 8650 Å satellite due to H-H⁺ interaction with an experimental profile. Line satellites can also be predicted in the Balmer- α line perturbed by neutral hydrogen.

The diatomic potentials and electronic transition moments among singlets and triplets exist for the Balmer- α line perturbed by collisions with neutral H; however, we have not previously reported our theoretical study of the wings of Balmer- α . Accounting for all transitions between $n_i = 2$ and $n_f = 3$ levels generates numerous molecular states that lead to the same asymptotic energy difference at $R \rightarrow \infty$. Of the total number, 36 asymptotically allowed transitions contribute to Balmer- α and 32 are forbidden. For the Lyman- α line, the triplet transitions contribute in the blue part of the profile and the singlet transitions in the red part of the profile. The line wings have been quantitatively examined for all of the components that contribute to the Balmer- α line. Our calculations allow us to identify which transition leads to a line satellite. Figure 9 shows the red satellite feature due to the $C 1^1\Pi_u \rightarrow 1^1\Delta_g$ centered at about 7800 Å in the red wing, whereas a close blue satellite is shown in Fig. 10. We restrict the present study to the blue wing. Figure 4 shows the short-range part of the repulsive potential curve of the $6^2\Sigma_u^+$ of the H-He molecule compared with the $6^3\Sigma_u^+$ state of the H₂ molecule. For H-H, the highest $6^3\Sigma_u^+$ is repulsive and leads to a maximum in the difference potential of the triplet transition $h^3\Sigma_g^+ \rightarrow 6^3\Sigma_u^+$ (Fig. 5), which is responsible for the formation of a blue line satellite at 1200 cm^{-1} . The resulting asymmetry of the Balmer- α line can be clearly seen in Fig. 10. The line shapes shown in

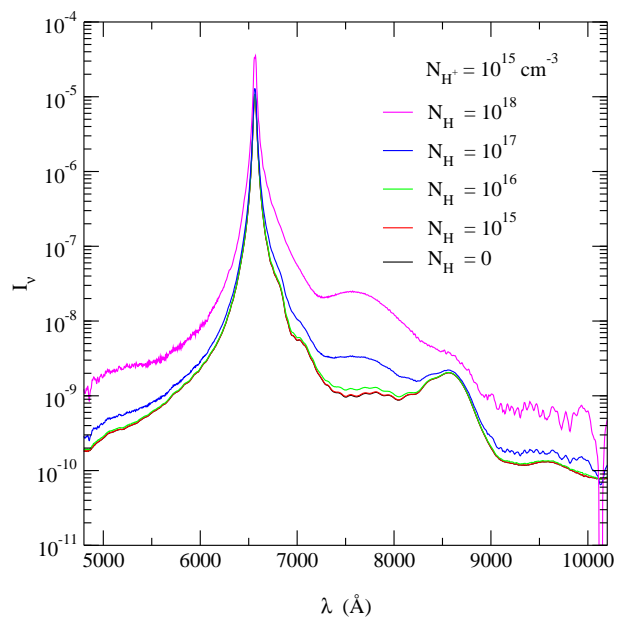


Fig. 9. Variation of the Balmer- α line perturbed by simultaneous collisions by protons and neutral H atom. The H⁺ density remains equal to 10^{15} cm^{-3} and the H density varies from 0 to 10^{18} cm^{-3} . The temperature is 10000 K.

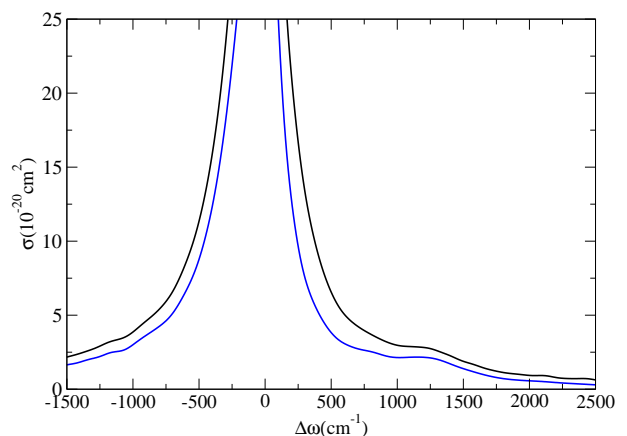


Fig. 10. Comparison of the Balmer- α line perturbed by H-H collisions (black curve) with the contribution of the triplet transitions alone (blue curve). The H density is 10^{18} cm^{-3} ; the temperature is 5000 K.

Figs. 10 and 6 are very similar, the blue H₂ line satellite being a little farther from the core of the line in the case of H-H collisions. When the H density increases from 10^{18} to 10^{21} cm^{-3} (Fig. 11) the satellite features appear as shoulders centered at about 7800 Å in the red wing and at 6100 Å in the blue wing. The H-H blue satellite is still apparent as a shoulder, whereas the H-He satellite is lost in the blue tail. They both emphasize the non-Lorentzian behavior on the blue side. The change from Lorentzian can be attributed entirely to radiation during close H-H and H-He collisions. In Fig. 11 in Allard et al. (2008) we compared our calculation of the unified theory line profile to the Lorentzian profile using the impact limit for the same H density 10^{18} cm^{-3} as in Fig. 10. The Lorentzian profile shown in Fig. 11

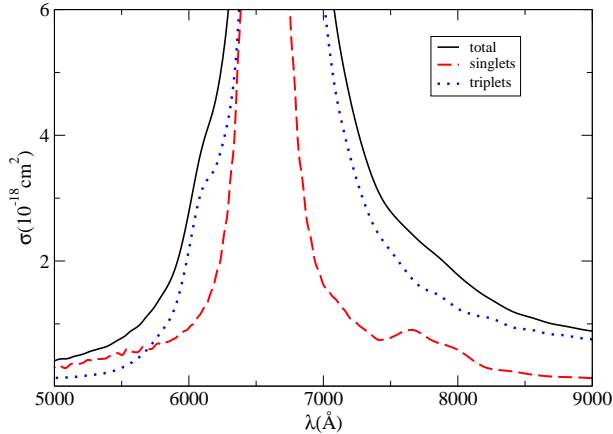


Fig. 11. Balmer- α line, perturbed by H-H collisions (black curve), and the Balmer line with the sole contribution of the triplet transitions (blue dotted curve) and the sole contribution of the singlet transitions (dashed red curve). The H density is 10^{21} cm^{-3} ; the temperature is 5000 K.

of Allard et al. (2008) is a useful representation of the unified line shape only from 6540 to 6580 Å.

5. General trend of the repulsive Σ states and conclusion

Spiegelman et al. (2021) made an exhaustive study of the blue asymmetry in the Lyman- α line profile perturbed by H-He and H-H collisions. In the present paper we have shown that a similar asymmetry exists for the Balmer- α line profile.

Figure 12 illustrates the repulsive potential energies and their difference $\Delta V(R)$ for the transitions $n_i \rightarrow n_f$ involved in Lyman- α and Balmer- α . Their importance must be noted in view of the study of the asymmetrical shape dependence on the order of the Balmer series. In the case of the Lyman- α and Balmer- α lines, among all molecular states correlated to a given atomic configuration, the highest ones in the configuration, namely $C^2\Sigma^+$ and $6^2\Sigma^+$ for H-He and $h^3\Sigma_g^+$ and $6^3\Sigma_u^+$ for H-H, are repulsive and have a prominent role in the appearance of features in the blue wing.

For $n_i=2 \rightarrow n_f$ with $n_f > 3$, the transitions that give rise to a blue satellite will be asymptotically forbidden.

Due to the more diffuse character of the $3s$, $3p$, and $3d$ orbitals in comparison with the $2s$ and $2p$, the barrier of state $6^2\Sigma^+$ extends to a wider distance range and is lower than that of state $C^2\Sigma^+$ (Fig. 12, top). The bottom plot of Fig. 12 shows that the maximum in ΔV occurs at larger internuclear distances ($R_{\text{max}} \sim 5.4 \text{ Å}$) for Balmer- α than for Lyman- α . This leads to an increase in the collision volume; the average number of perturbers in the interaction volume at R_{max} is the determining parameter for the amplitude of the satellites on the spectral line (Allard 1978; Royer 1978; Allard & Kielkopf 1982). This dependence on the average number of perturbers in the collision volume is expected on the basis of the Poisson distribution, which indicates the probability of finding a given number of uncorrelated perturbers in the collision volume. It was identified decisively in the theoretical analysis of experimental Cs spectra by Kielkopf & Allard (1979).

For the H-He Balmer- α line, the maximum ΔV_{max} is smaller, 1000 cm^{-1} versus 5000 cm^{-1} for the Lyman- α line (Fig. 12, bottom). The Balmer line satellite is then closer to the main line than

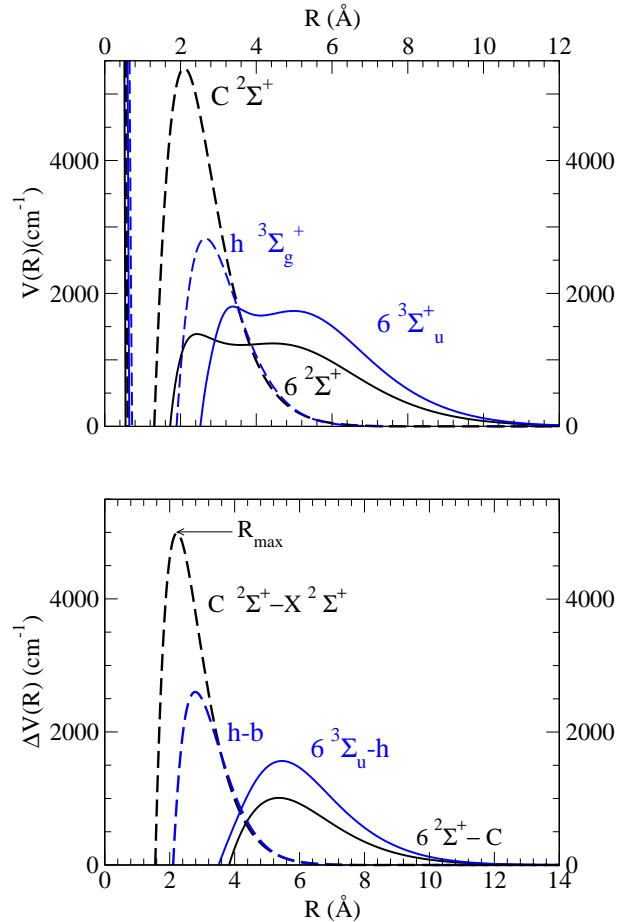


Fig. 12. Repulsive potentials and their difference for H-He and H-H. Top: Potential energy V of the repulsive states of Balmer- α perturbed by H-He collisions (black curves); H-H collisions (blue curves); and the same, but for Lyman- α (dashed curves). Bottom: Difference potential $\Delta V(R)$ for the Balmer transitions $6^2\Sigma^+-C^2\Sigma^+$ of H-He collisions (black curves); $6^3\Sigma_u^+-h^3\Sigma_g^+$ of H-H collisions (blue curves); and the same, but for the Lyman (dashed curves) $C^2\Sigma^+-X^2\Sigma^+$ and $h^3\Sigma_g^+-b^3\Sigma_u^+$ transitions.

the Lyman satellite, as shown in Fig. 6 and Fig. 11 of Spiegelman et al. (2021). Because of this general trend characterizing the repulsive Σ states, the average number of perturbers in the interaction volume will be larger for higher series of Balmer lines leading to a higher probability of multiple perturber effects that give rise to the long blue tail due to the closer relative proximity of the satellite band to the line.

This effect can be unimportant when the perturber density is low, whereas it becomes dramatic when this density can be as large as 10^{21} cm^{-3} in the cool atmosphere of DZA white dwarfs. The Balmer- α line profile shown in Fig. 11 is purely formal as we do not reach this H density in cool stars, but was essentially done for our comparison H-He versus H-H.

For the higher series of Balmer lines we can predict that the main line is not a Lorentzian, but is replaced by a blend of multiple satellites (Kielkopf 1983, 1985). We have shown (Fig. 7) that the Balmer- α line core is no longer a Lorentzian when the He density is as high as 10^{21} cm^{-3} .

When the helium density is as large as it is in the DZA stars such as L745-46A, only the Balmer- α line is observed and it is very shallow. For cooler WD when the helium density is even

higher, Balmer lines are extremely weak or totally absent as in extreme helium stars. We have conclusively shown the need for precise accurate and complete profiles of neutral collision-broadened lines when hydrogen abundances are found from their profiles in stellar spectra.

Acknowledgements. NFA is grateful to M. Leseignoux, C. Giovanetti, A. Lekic, F. Lanzi, B. Pape and A. Dereu for their help in the analysis of the huge number of molecular transitions which contribute to the Balmer- α line perturbed by collisions with neutral H. We thank the referee for helpful comments and P. Bonifacio for references of 3D calculations.

References

- Ali, A. W. & Griem, H. R. 1966, *Physical Review*, 144, 366
- Allard, N. F. 1978, *J. Phys. B: At. Mol. Opt. Phys.*, 11, 1383
- Allard, N. F., Drira, I., Gerbaldi, M., Kielkopf, J. F., & Spielfiedel, A. 1998, *A&A*, 335, 1124
- Allard, N. F. & Kielkopf, J. F. 1982, *Rev. Mod. Phys.*, 54, 1103
- Allard, N. F., Kielkopf, J. F., & Allard, F. 2007, *EPJ D*, 44, 507
- Allard, N. F., Kielkopf, J. F., Cayrel, R., & van 't Veer-Menneret, C. 2008, *A&A*, 480, 581
- Allard, N. F., Kielkopf, J. F., Xu, S., et al. 2020, *MNRAS*, 494, 868
- Allard, N. F., Royer, A., Kielkopf, J. F., & Feautrier, N. 1999, *Phys. Rev. A*, 60, 1021
- Amarsi, A. M., Nordlander, T., Barklem, P. S., et al. 2018, *A&A*, 615, A139
- Barklem, P. S., Piskunov, N., & O'Mara, B. J. 2000a, *A&A*, 363, 1091
- Barklem, P. S., Piskunov, N., & O'Mara, B. J. 2000b, *A&A*, 355, L5
- Barklem, P. S., Stempels, H. C., Allende Prieto, C., et al. 2002, *A&A*, 385, 951
- Brooks, R. L. & Hunt, J. L. 1988, *The Journal of Chemical Physics*, 89, 7077
- Cayrel, R., van 't Veer-Menneret, C., Allard, N. F., & Stehlé, C. 2011, *A&A*, 531, A83
- Cukanovaite, E., Tremblay, P.-E., Bergeron, P., et al. 2021, *MNRAS*, 501, 5274
- Giribaldi, R. E., Ubaldo-Melo, M. L., Porto de Mello, G. F., et al. 2019, *A&A*, 624, A10
- Ketterle, W. 1989, *Phys. Rev. Lett.*, 62, 1480
- Ketterle, W. 1990a, *The Journal of Chemical Physics*, 93, 3752
- Ketterle, W. 1990b, *The Journal of Chemical Physics*, 93, 3760
- Ketterle, W. 1990c, *The Journal of Chemical Physics*, 93, 6935
- Ketterle, W., Dodhy, A., & Walther, H. 1988, *The Journal of Chemical Physics*, 89, 3442
- Ketterle, W., Figger, H., & Walther, H. 1985, *Phys. Rev. Lett.*, 55, 2941
- Kielkopf, J. 1983, *Journal of Physics B Atomic Molecular Physics*, 16, 3149
- Kielkopf, J. 1985, *J. Quant. Spectr. Rad. Transf.*, 33, 267
- Kielkopf, J. F. & Allard, N. F. 1979, *Physical Review Letters*, 43, 196
- Kielkopf, J. F. & Allard, N. F. 2014, *Journal of Physics B Atomic Molecular Physics*, 47, 155701
- Kielkopf, J. F., Allard, N. F., & Decrette, A. 2002, *European Physical Journal D*, 18, 51
- Knowles, P. & Werner, H.-J. 1992, *Theoretica Chim. Acta*, 84, 95–103
- Koester, D. & Wolff, B. 2000, *A&A*, 357, 587
- Kramida, A., Yu. Ralchenko, Reader, J., & and NIST ASD Team. 2020, *NIST Atomic Spectra Database (ver. 5.8)*, [Online]. Available: <https://physics.nist.gov/asd> [2021, January 26]. National Institute of Standards and Technology, Gaithersburg, MD.
- Lo, J. M. H., Klobukowski, M., Bielińska-Waz, D., Schreiner, E. W. S., & Dierksen, G. H. F. 2006, *Journal of Physics B: Atomic, Molecular and Optical Physics*, 39, 2385
- Ludwig, H. G., Behara, N. T., Steffen, M., & Bonifacio, P. 2009, *A&A*, 502, L1
- Nakajima, T. & Hirao, K. 2011, *Chemical reviews*, 112, 385
- Peach, G. 2011, *Baltic Astronomy*, 20, 516
- Petsalakis, I. D., Theodorakopoulos, G., & Buenker, R. J. 1990, *The Journal of Chemical Physics*, 92, 4920
- Reiher, M. 2006, *Theoretical Chemistry Accounts*, 116, 241–252
- Royer, A. 1978, *Acta Phys. Pol. A*, 54, 805
- Sarpal, B. K., Branchett, S. E., Tennyson, J., & Morgan, L. A. 1991, *Journal of Physics B: Atomic, Molecular and Optical Physics*, 24, 3685
- Spiegelman, F., Allard, N., & Kielkopf, J. 2021, *A&A*, 651, A51
- Spielfiedel, A. 2003, *J. Mol. Spectrosc.*, 217, 162
- Spielfiedel, A., Palmieri, P., & Mitrushenkov, A. 2004, *Molec. Phys.*, 102, 2249
- Theodorakopoulos, G., Petsalakis, I. D., Nicolaidis, C. A., & R.J.Buenker. 1987, *J. Phys. B*, 20, 2339
- Unsöld, A. 1955, *Physik der Sternatmosphären MIT besonderer Berücksichtigung der Sonne* (Berlin, Springer, 1955. 2. Aufl.)
- van Hemert, M. C. & Peyerimhoff, S. D. 1991, *The Journal of Chemical Physics*, 94, 4369
- Werner, H.-J., Knowles, P. J., Knizia, G., et al. 2015, *MOLPRO*, version 2015.1, a package of ab initio programs
- Xu, S., Zuckerman, B., Dufour, P., et al. 2017, *ApJ*, 836, L7

Appendix A: Spectroscopic constants of molecular states of HeH correlated with H(n=3)Table A.1. Spectroscopic constants of HeH adiabatic molecular states dissociating into H(3s,3p,3d)+He(1s²).

State	ref	R_e (Å)	ω_e (cm ⁻¹)	ω_{exe} (cm ⁻¹)	ω_{eye} (cm ⁻¹)	D_e (eV/cm ⁻¹)	T_e (cm ⁻¹)	T_{00} (cm ⁻¹)
4 ² Σ^+	(a)	0.7640	3382.7	162.8	42.4	2.172/17517.8	18382.2	18207.0
	(b)	0.7675	3383					
	(c)	0.7677	3187					
	(d)	0.7702	3405	201		2.16		
	(e)	0.7709	3346.0	167.3		2.139/17255.6		
	(f)							18215.24
5 ² Σ^+	(a)	0.7759	3228.1	148.4	57.5	2.066/16674.1	19225.6	18979.3
	(c)	0.7775	3057					
	(d)	0.7816	3252	208		2.06		
	(e)	0.7832	3148.5	141.1		2.032/16394.8		
	(f)							18945.92
6 ² Σ^+	(a)	0.7851	3148.6	168.3	31.1	1.680/13554.5	22345.7	22050.7
	(e)	0.7921	3094.3	149.5		1.6522/13321.7		
2 ² Π	(a)	0.7727	3267.6	178.4	22.1	2.096/16908	18991.9	18752.7
	(b)	0.7788	3233					
	(c)	0.7755	3083					
	(d)	0.7783	3299	207		2.08		
	(e)	0.7833	3157.3	152.7		2.018/16274.7		
	(f)							18762.32
3 ² Π	(a)	0.7750	3239.2	175.1	24.6	2.057/16588	19311.9	19059.7
	(e)	0.7799	3174.2	143.3		2.045/16496.1		
	(f)							19023.31
1 ² Δ	(a)	0.7738	3251.2	177.4	23.3	2.034/16406	19506.0	19259.0
	(e)	0.7810	3195.1	154.3		1.986/16020.8		
	(f)							19248.90

Electronic dissociation energies D_e are calculated with reference to the respective dissociation limits of the adiabatic states. T_e is the electronic transition energy from state $A^2\Sigma^+$, T_{00} the associated $v'=0$ to $v''=0$ transition. The present vibrational data were determined for ⁴HeH through five-point polynomial interpolation. References: (a) theory, this work; (b) theory, Theodorakopoulos et al. (1987); (c) theory, Sarpal et al. (1991); (d) theory, Lo et al. (2006); (e) theory, van Hemert & Peyerimhoff (1991); (f) experiment, Ketterle (1990b).